The Astrophysical Journal, 831:61 (10pp), 2016 November 1 doi:10.3847/0004-637X/831/1/61

DYNAMICS OF TIDALLY CAPTURED PLANETS IN THE GALACTIC CENTER

Alessandro A. Trani[1,2], Michela Mapelli[2], Mario Spera[2], and Alessandro Bressan[1,2]
[1] Scuola Internazionale Superiore di Studi Avanzati (SISSA), Via Bonomea 265, I-34136, Trieste, Italy; aatrani@gmail.com
[2] INAF-Osservatorio Astronomico di Padova, Vicolo dell'Osservatorio 5, I-35122, Padova, Italy
Received 2016 July 13; revised 2016 August 17; accepted 2016 August 19; published 2016 October 27

ABSTRACT

Recent observations suggest ongoing planet formation in the innermost parsec of the Galactic center. The supermassive black hole (SMBH) might strip planets or planetary embryos from their parent star, bringing them close enough to be tidally disrupted. Photoevaporation by the ultraviolet field of young stars, combined with ongoing tidal disruption, could enhance the near-infrared luminosity of such starless planets, making their detection possible even with current facilities. In this paper, we investigate the chance of planet tidal captures by means of high-accuracy *N*-body simulations exploiting Mikkola's algorithmic regularization. We consider both planets lying in the clockwise (CW) disk and planets initially bound to the S-stars. We show that tidally captured planets remain on orbits close to those of their parent star. Moreover, the semimajor axis of the planetary orbit can be predicted by simple analytic assumptions in the case of prograde orbits. We find that starless planets that were initially bound to CW disk stars have mild eccentricities and tend to remain in the CW disk. However, we speculate that angular momentum diffusion and scattering by other young stars in the CW disk might bring starless planets into orbits with low angular momentum. In contrast, planets initially bound to S-stars are captured by the SMBH on highly eccentric orbits, matching the orbital properties of the clouds G1 and G2. Our predictions apply not only to planets but also to low-mass stars initially bound to the S-stars and tidally captured by the SMBH.

Key words: black hole physics – Galaxy: center – methods: numerical – planet–star interactions – planets and satellites: dynamical evolution and stability

1. INTRODUCTION

Several hundred young stars lie in the innermost parsec of our Galactic center (GC). The orbits of the so-called S-stars, ∼28 young (≈20–100 Myr) stars lying close (<0.04 pc) to the supermassive black hole (SMBH), provide the strongest constraints on its mass (Ghez et al. 2003; Schodel et al. 2003; Gillessen et al. 2009). The S-stars have been classified as B-type stars and have randomly oriented, highly eccentric orbits. Hundreds of young (∼2–6 Myr) stars (mainly Wolf–Rayet and O-type stars, Paumard et al. 2006; Lu et al. 2009, 2013) lie further out (>0.04 pc), 20% of which form a nearly Keplerian disk around the SMBH, named the clockwise (CW) disk for its motion when projected on the plane of the sky (Bartko et al. 2009; Yelda et al. 2014). The formation mechanisms and dynamical evolution of such stars are still debated, since the tidal field of the SMBH is expected to disrupt molecular clouds in the innermost parsec (e.g., Bonnell & Rice 2008; Mapelli et al. 2008, 2012; Hobbs & Nayakshin 2009; Alig et al. 2011, 2013; Lucas et al. 2013; Mapelli & Trani 2016; Trani et al. 2016, see Mapelli & Gualandris 2016 for a review).

Young stars in the local universe are often surrounded by a protoplanetary disk (e.g., Williams & Cieza 2011 for a review). Thus, it is likely that protoplanetary disks exist even in the GC, despite the environment being quite hostile to star and planet formation. Indeed, recent radio continuum observations suggested the presence of photoevaporating protoplanetary disks in the innermost ∼0.1 pc (Yusef-Zadeh et al. 2015). Whether planets can form in such protoplanetary disks is still highly uncertain.

Mapelli & Ripamonti (2015) recently showed that starless planets are too faint to be observed in the GC with current facilities, even if they are photoevaporated by the intense ultraviolet (UV) emission of the young massive stars. However, if a planet or protoplanetary embryo is undergoing tidal disruption by the field of the SMBH, the efficiency of photoevaporation can be enhanced by orders of magnitude: a Brγ luminosity of $\approx 10^{31}$ erg s^{-1} can be emitted in this case, observable with 10 m class telescopes (Mapelli & Ripamonti 2015). Moreover, high-energy flares with a luminosity of $\leqslant 2 \times 10^{41}$ erg s^{-1} can be associated with tidal disruption events of planets by SMBHs (Zubovas et al. 2012). The tidal disruption of smaller bodies, such as asteroids or planetesimals, is expected to be very frequent (although less energetic than that of planets), and has been invoked to explain the daily infrared flares of Sgr A* (Čadež et al. 2008; Kostić et al. 2009; Zubovas et al. 2012; Hamers & Portegies Zwart 2015).

Finally, a protoplanetary origin has been suggested even for the dusty object G2, which has been observed to orbit the SMBH on a highly eccentric orbit ($e \sim 0.98$) with extremely small pericenter ($a \sim 200$ au, Gillessen et al. 2011, 2013a, 2013b; Eckart et al. 2013; Phifer et al. 2013; Witzel et al. 2014; Pfuhl et al. 2015). In fact, Murray-Clay & Loeb (2012) proposed that G2 is a low-mass star with a protoplanetary disk, while Mapelli & Ripamonti (2015) suggested that the properties of G2 are consistent with a planetary embryo tidally captured by the SMBH. The origin of G2 is still debated, and many other theories have been proposed to explain it: a gas cloud formed by colliding stellar winds (Burkert et al. 2012; Schartmann et al. 2012; Gillessen et al. 2013a; Shcherbakov 2014; Calderón et al. 2016) or tidally stripped material (Guillochon 2016), the merger product of a binary (Prodan et al. 2015), a low-mass star obscured by dust (Ballone et al. 2013; Scoville & Burkert 2013; De Colle et al. 2014; Witzel et al. 2014), a star disrupted by a stellar black hole (Miralda-Escudé 2012), and a nova outburst (Meyer & Meyer-Hofmeister 2012). Moreover, another similar object, named G1 (Clénet et al. 2005; Ghez et al. 2005), has been suggested by Pfuhl et al. (2015) to share the same origin as G2. The orbit of G1

has lower eccentricity ($e \sim 0.93$) and smaller semimajor axis ($a \sim 2970$ au), but is very similar to that of G2.

In conclusion, whether planets and protoplanets exist in the GC is still an open question, and their detection with current facilities is challenging. Our aim is to study the dynamics of planets and protoplanets near the SMBH in the GC, in order to put constraints on future observations. In particular, we study the tidal capture of hypothetical planets and protoplanets orbiting stars in the CW disk and in the S-star cluster. We simulate hierarchical three-body systems composed of a SMBH, a star, and a planet. In our three-body runs the orbit of the star around the SMBH is randomly sampled according to the properties of the CW disk. We also simulate the entire S-star cluster, adding a planet to each simulated S-star. In Section 2 we describe the methodology we employed for our simulations; in Section 3 we present our results. In Section 4, we discuss the implications of our work. Our conclusions are presented in Section 5.

2. METHODS

2.1. Mikkola's Algorithmic Regularization Code

Modeling the evolution of planets close to the SMBH is challenging, because of the extreme mass ratios involved. Thus, our simulations are run by means of a fully regularized *N*-body code that implements the Mikkola's algorithmic regularization (MAR, Mikkola & Tanikawa 1999a, 1999b). This code is particularly suitable for studying the dynamical evolution of few-body systems in which strong gravitational encounters are very frequent and the mass ratio between the interacting objects is large. The MAR scheme removes the singularity of the two-body gravitational potential for $r \to 0$, by means of a transformation of the time coordinate (see Mikkola & Tanikawa 1999a for the details).

Our implementation uses a leapfrog scheme in combination with the Bulirsh–Stoer extrapolation algorithm (Stoer & Bulirsch 2002) to increase the accuracy of the numerical results. The code integrates the equations of motion, employing relative coordinates by means of the so-called chain structure. This change of coordinates reduces round-off errors significantly (Aarseth 2003). At present, this code is a submodule of the direct *N*-body code HiGPUs-R, which is still under development (M. Spera 2016, in preparation; see Capuzzo-Dolcetta et al. 2013 for the current non-regularized version of HiGPUs). Still, it can be used as a stand-alone tool to study the dynamical evolution of few-body systems with very high precision.

Tidal dissipation is not taken into account in the current version of the code. In fact, we expect the effect of tidal dissipation to be negligible in our simulations, since the timescale of orbital decay is $\approx$1 Gyr, much longer than the length of our simulations (10^3–10^4 yr).

2.2. CW Disk Simulations

Simulating the entire CW disk (>1000 stars) in the same run is prohibitive for MAR codes. Thus, we run simulations of a three-body hierarchical system composed of a SMBH, a star, and a planet initially bound to the star. We set the masses of the SMBH, star, and planet to $4.31 \times 10^6\,M_\odot$ (Gillessen et al. 2009), $5\,M_\odot$, and $10\,M_{\rm Jup}$, respectively, where $M_{\rm Jup}$ is the mass of Jupiter. The stellar orbit around the SMBH is modeled following the properties of the stars in the CW disk.

Table 1
Main Properties of the Simulations of Planets in the CW Disk

Set	Orbit of Planet	N	$N_{\rm unb}$
A	Coplanar, prograde	10^4	8903
B	Coplanar, retrograde	10^4	6488
C	Inclined, prograde	10^4	8817
D	Inclined, retrograde	10^4	7791

Note. Column 1: set name; column 2: spin of the planetary orbit with respect to the stellar orbit; column 3: number of realizations; column 4: number of realizations in which the planet becomes unbound with respect to the parent star.

The semimajor axis is drawn from a power-law distribution with index $\Gamma = 1.93$ (Do et al. 2013), in the range 0.03–0.06 pc, corresponding to the inner edge of the CW disk (planets orbiting CW stars on outer orbits are less likely to be affected by the tidal field of the SMBH). The stellar eccentricity is drawn from a Gaussian distribution centered at 0.3 with $\sigma = 0.1$.

A planet will likely remain bound to the star if its distance from the star is less than Jacobi radius $r_{\rm J}$ of the star–planet system:

$$r_{\rm J} = d\left(\frac{m}{3M_{\rm SMBH}}\right)^{1/3}, \quad (1)$$

where $M_{\rm SMBH}$ is the mass of the SMBH, m is the total mass of the star–planet system, and d is the distance between the star and the SMBH.

With these initial conditions we expect the Jacobi radius to be in the range 20–90 au. We assume that the planetary orbit around the star is circular with radius in the uniform range 10–100 au. Planets with a semimajor axis smaller than 10 au are unlikely to be captured by the SMBH, while planets with semimajor axis larger than 100 au will already be unbound from the star. We set the eccentricity of the planetary orbit to zero in order to prevent the parameter space from exploding. On the other hand, we expect that planets on eccentric orbits escape even faster.

We consider different inclinations with respect to the stellar orbit: coplanar prograde orbits ($i = 0°$, set A), coplanar retrograde orbits ($i = 180°$, set B), inclined prograde orbits (uniformly distributed over $i < 90°$ or $> 270°$, set C), and inclined retrograde orbits (uniformly distributed over $90° < i < 270°$, set D). The mean anomalies of star and planet are uniformly distributed between 0° and 360°. We run 10^4 realizations for each set and stop the simulations at 10^4 yr. Table 1 shows a summary of the simulation sets presented in this paper.

2.3. S-star Simulations

Unlike the CW disk, the S-star cluster is sufficiently small to be simulated in the same run with the MAR algorithm. We run simulations of the 27 innermost S-stars for which the orbital elements are known, using as initial conditions the orbital parameters reported by Gillessen et al. (2009). We assign to each star a planet of $10\,M_{\rm Jup}$ in a circular orbit. The planetary semimajor axis ranges between 1 and 20 au, distributed in 20 equally spaced bins. For each semimajor axis we run 1000 realizations, randomizing the orientation of the planetary orbit

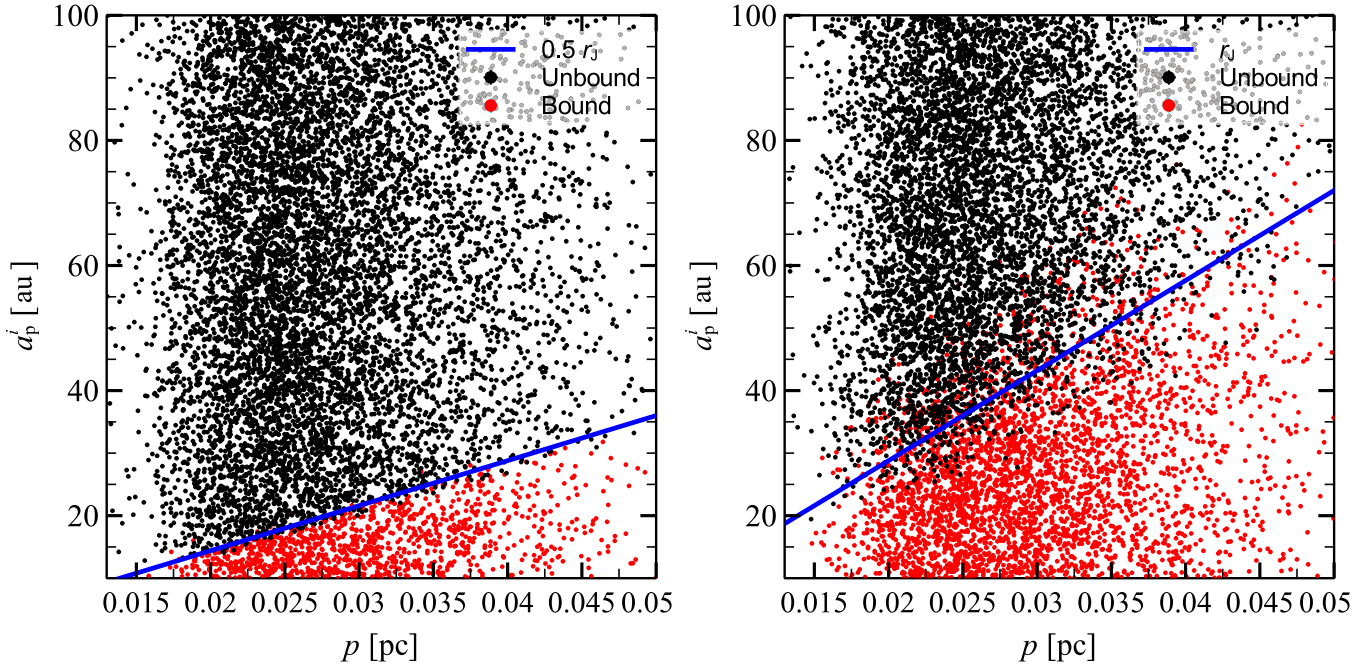

Figure 1. Initial semimajor axis of the planet vs. pericenter distance of the stellar orbit. Each dot represents a single realization of a three-body system of set A (coplanar prograde, left panel) and set B (coplanar retrograde, right panel). Red dots: realizations in which the planet remains bound to the star throughout the simulation. Black dots: realizations in which the planet becomes unbound with respect to the star. Blue solid line: Jacobi radius (Equation (1)), multiplied by 0.5 in the left panel.

over the sphere, to give a total of 20,000 realizations. We stop the simulations at 1000 yr.

3. RESULTS

3.1. Planets in the CW Disk

In 88%–89% of the prograde runs (sets A and C) the planet escapes from the star and starts orbiting the SMBH. The escape fraction in retrograde runs (sets B and D) is lower: 65% and 78% of planets are tidally captured by the SMBH in set B and set D, respectively (see Table 1).

Figure 1 shows the initial semimajor axis of the planet a_p^i versus the pericenter distance p of the stellar orbit for set A (coplanar prograde, left panel) and set B (coplanar retrograde, right panel). The colors indicate whether the planet remains bound to its parent star throughout the simulations.

The unbound and bound regions in the a_p^i–p plane are clearly distinct. The boundary between the two regions scales linearly with p, as expected from the linear dependence of the Jacobi radius r_J on the star–SMBH distance (Equation (1)).

In the case of set A (Figure 1, left panel) the boundary is 0.5 r_J. In the case of set B (Figure 1, right panel) the boundary is $\sim$1 r_J. The boundary is $\sim$0.5 r_J and $\sim$0.9 r_J for sets C and D, respectively. Thus, the boundary radius is smaller for prograde orbits than for retrograde orbits. This difference is connected with the direction of the Coriolis force. Moreover, the boundary is less sharp in the case of retrograde orbits. This likely occurs because retrograde planets spend several periods at radius $\sim r_J$ without escaping, thanks to the stabilizing effect of the Coriolis force. In contrast, prograde planets escape immediately outside $0.5r_J$. As a consequence, planets in retrograde orbits are more affected by perturbations from the tidal field, which is stronger at larger distances from the star (Hamilton & Burns 1991, 1992).

Figure 2 shows the trajectory of a planet in a single simulation of set A (coplanar and prograde, left panel) and set B (coplanar and retrograde, right panel). The reference frame corotates with the star in its motion around the SMBH, so that the SMBH is always directed toward the negative x-axis. In the left panel, the orbit is initially within half of the Jacobi radius and the planet completes an orbit around the star before being captured by the SMBH. However, as the star moves toward its pericenter, the Jacobi radius of the system shrinks and the planet is captured by the tidal forces of the SMBH.

In the case of retrograde orbits (Figure 2, right panel), the trajectory of the planet can be much more convoluted. In this case, the orbit becomes unstable after the third pericenter passage of the parent star around the SMBH; the orbit of the planet becomes prograde before escaping from the Hill sphere of the star. Moreover, the Hill sphere at the initial time is smaller than that at the moment of planet escape, indicating that planet escape does not occur at pericenter passage. For more details about the temporary orbit of simulated planets see the Appendix.

Figure 3 shows the orbital properties of the planets after they are captured by the SMBH. In 95% of the runs of set A (Figure 3, top-left panel) the semimajor axis of the planet a_p (with respect to the SMBH) differs by less than 7% from the semimajor axis of its parent star a_s.

The small difference between a_p and a_s is a result of the change in the orbital energy of the planet being of the same order of magnitude as the binding energy of the star–planet system (E_{sp}). For our assumptions, $E_{sp} \approx 10^{43}$ erg. This is much smaller than the binding energy between the star and the SMBH ($\approx 10^{49}$ erg), indicating that the recoil velocity acquired by the planet during the capture event is much smaller than its initial velocity with respect to the SMBH.

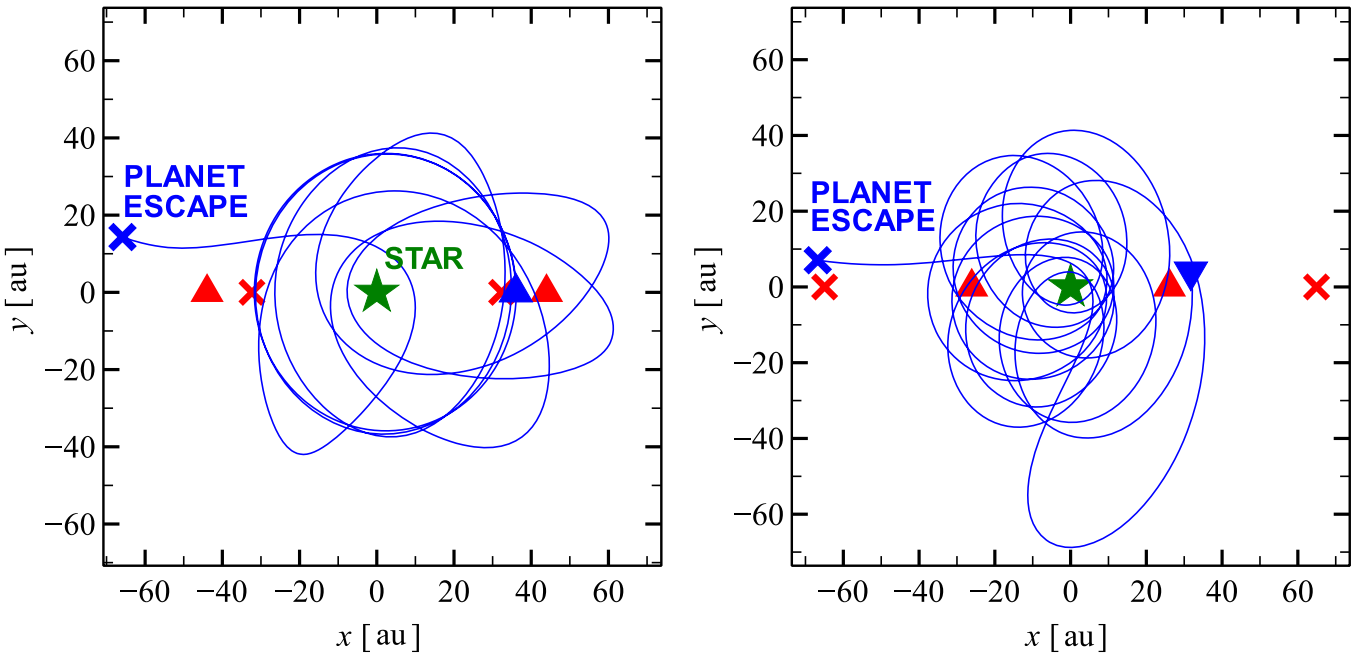

Figure 2. Trajectory of the planet in the reference frame that corotates with the star for a single simulation of set A (left panel) and set B (right panel). The negative x-axis points always toward the SMBH, while the tangential velocity of the star lies along the positive y-axis. Blue solid line: trajectory of the planet. Blue triangle: initial position of the planet. Blue cross: position of the planet at the time the planet becomes unbound with respect to the star. Green star: position of the star. Red triangle: initial Jacobi radius of the system (Equation (1)), multiplied by 0.5 in the left panel. Red cross: same as red triangle, but at the time the planet becomes unbound with respect to the star.

The gap in the semimajor axis distribution in the top-left panel of Figure 3 indicates that the semimajor axis of the escaped planet is never equal to the semimajor axis of the parent star. The gap becomes wider as the eccentricity of the planetary orbit deviates from that of the parent star.

The eccentricity distribution depends on whether the planet has a smaller or larger semimajor axis than that of the parent star. In the case of smaller semimajor axis, the eccentricity distribution is centered at a lower eccentricity relative to the parent star, while in the case of larger semimajor axis the eccentricity distribution is centered at a higher one. In 95% of the runs of set A the eccentricity of the planetary orbit e_p differs by less than 15% from the eccentricity of its parent star e_s.

In runs of set B (retrograde coplanar runs, see Figure 3, top-right panel), the distribution of the semimajor axis of planets normalized to that of stars with respect to the SMBH (a_p/a_s) has no gaps. The spread in semimajor axis is lower than in set A, while the spread of eccentricities is higher. As in set A, tighter planetary orbits tend to have higher eccentricity and vice versa.

The bottom panels of Figure 3 show the orbital properties of the planets for the runs of set C (inclined and prograde, bottom-left panel) and set D (inclined and retrograde, bottom-right panel). Inclined orbits follow the same trend as coplanar ones: runs of set C exhibit a gap in the a_p/a_s distribution, while runs of set D show no gap.

About 51% of runs of sets A and C (prograde runs) have $a_p < a_s$. In contrast, just 45% and 43% of runs of sets B and D (retrograde runs) have $a_p < a_s$, respectively. In the retrograde runs, the planets tend to end up on orbits less bound than those of their parent star.

Figure 4 shows the ratio a_p/a_s between the semimajor axis of the planet and that of the parent star versus the orbital phase φ_p of the planet at the first pericenter passage of the star. We predict the orbital phase analytically using the initial conditions of each realization. From the left panel of Figure 4 it is apparent that the planet will likely have a semimajor axis smaller than that of its parent star ($a_p/a_s < 1$) in runs of set A if it is in between the SMBH and the star during the stellar pericenter passage ($\varphi_p \simeq 180°$). In contrast, the planet will likely have a semimajor axis larger than that of its parent star ($a_p/a_s > 1$) if the planet is on the opposite side of the orbit with respect to the SMBH ($\varphi_p \simeq 0°$). Figure 5 is a schematic representation of this result. The same trend is still present (but much less evident) in runs of set B (Figure 4, right panel).

We find that the planet may undergo a close encounter with the star during its orbit around the SMBH. This occurs because the planet remains on an orbit similar to that of its parent star, so that it may encounter the star again after one synodic period. However, since the difference between the orbital periods of the star and the planet is small, the synodic period is $\gtrsim$5000 yr. On this timescale, perturbations from nearby stars might become non-negligible before the planet undergoes the encounter with its parent star.

3.2. Planets in the S-star Cluster

Figure 6 shows the fraction of captured and ejected planets versus the initial semimajor axis of planetary orbits for all the S-star simulations. As expected, the fraction of unbound planets increases with the initial semimajor axis. 57% of the planets in our simulations get captured by the SMBH. In total 0.18% of the planets get ejected from the system. The fraction of ejected planets decreases for larger initial semimajor axis. This is expected: the larger the semimajor axis, the smaller the binding energy of the planet–star system that can be released as recoil velocity during the encounter with the SMBH.

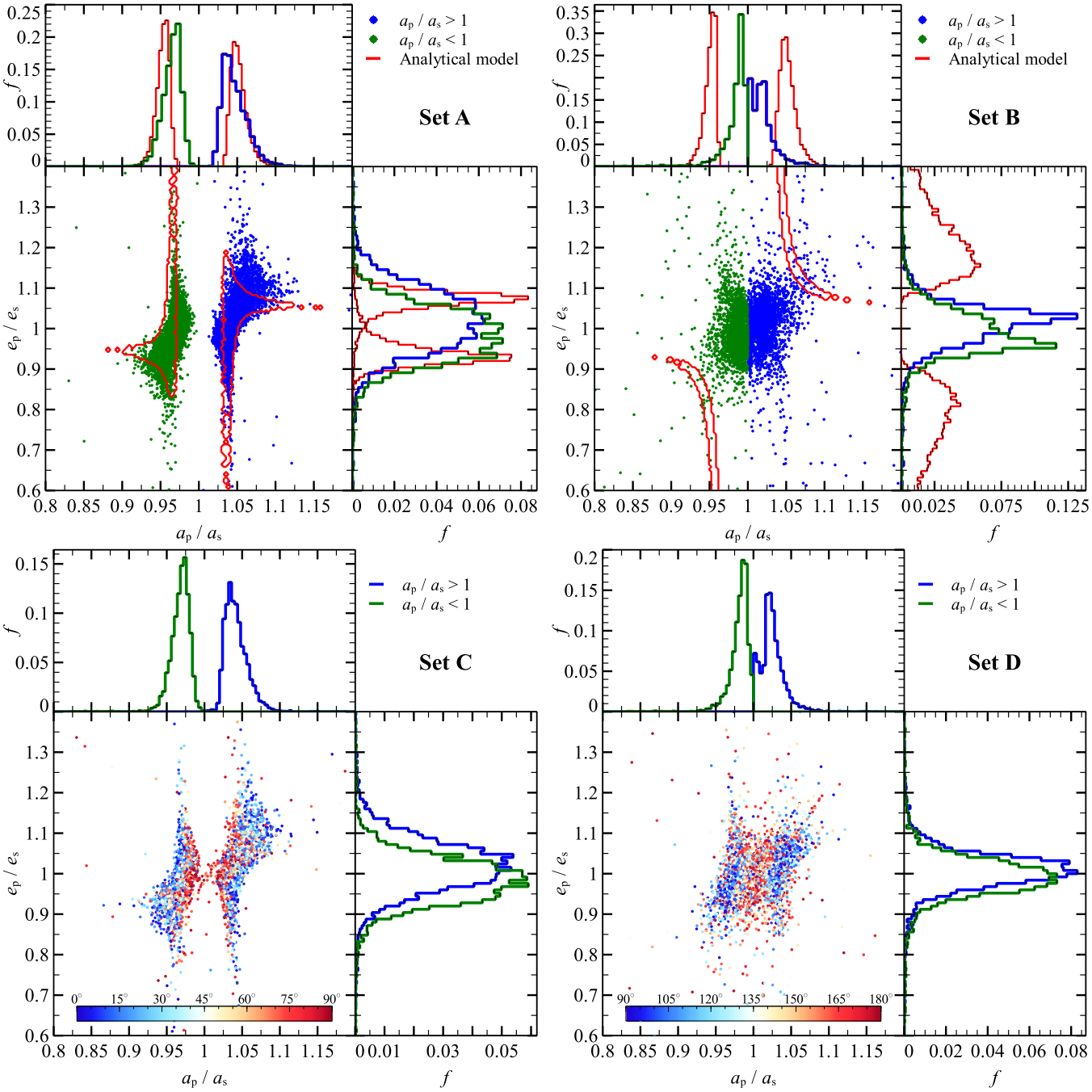

Figure 3. Semimajor axis of the planetary orbit (around the SMBH) normalized to the semimajor axis of the stellar orbit a_p/a_s vs. eccentricity of the planetary orbit (around the SMBH) normalized to the eccentricity of the stellar orbit e_p/e_s. In the top panels: blue dots indicate realizations in which the semimajor axis of the planet is larger than that of its parent star ($a_p/a_s > 1$); green dots indicate realizations in which the semimajor axis of the planet is smaller than that of its parent star ($a_p/a_s < 1$); red contours indicate predictions of the analytic model (Equation (2)). In the bottom panels: the color map indicates the inclination of the planetary orbit with respect to the stellar orbit. $i = 0°$, 90°, and 180° correspond to prograde coplanar orbits, normal orbits, and retrograde coplanar orbits, respectively. In all panels: green histograms indicate the distributions of planets with $a_p/a_s < 1$, while blue histograms indicate the distributions of planets with $a_p/a_s > 1$. Top-left panel: set A (coplanar prograde runs). Top-right panel: set B (coplanar retrograde runs). Bottom-left panel: set C (inclined prograde runs). Bottom-right panel: set D (inclined retrograde runs).

Figure 7 shows the trajectory of a planet around star S19, in the rotating reference frame that corotates with the star. The stellar orbit lies in the x–y plane, and the negative x-axis is always directed toward the SMBH. The orbit of the planet has an initial radius of 10 au and it is inclined by 20° with respect to the stellar orbit. The orbit of the planet immediately becomes eccentric ($e \simeq 0.8$) due to the strong tidal forces and acquires an inclination of 45° and a semimajor axis of 8 au. The orbit remains stable around the star for several periods, until the planet is kicked into a looser orbit with $i \simeq 100°$, $a \simeq 20$ au, and $e \simeq 0.3$. After 260 yr, the planet escapes along the negative x-axis and gets captured by the SMBH.

The morphology of planetary orbits varies greatly from simulation to simulation. Flips of planetary orbit may occur, with the planet spending time on several temporarily stable orbits around the star before escaping. In Section 4.2 we

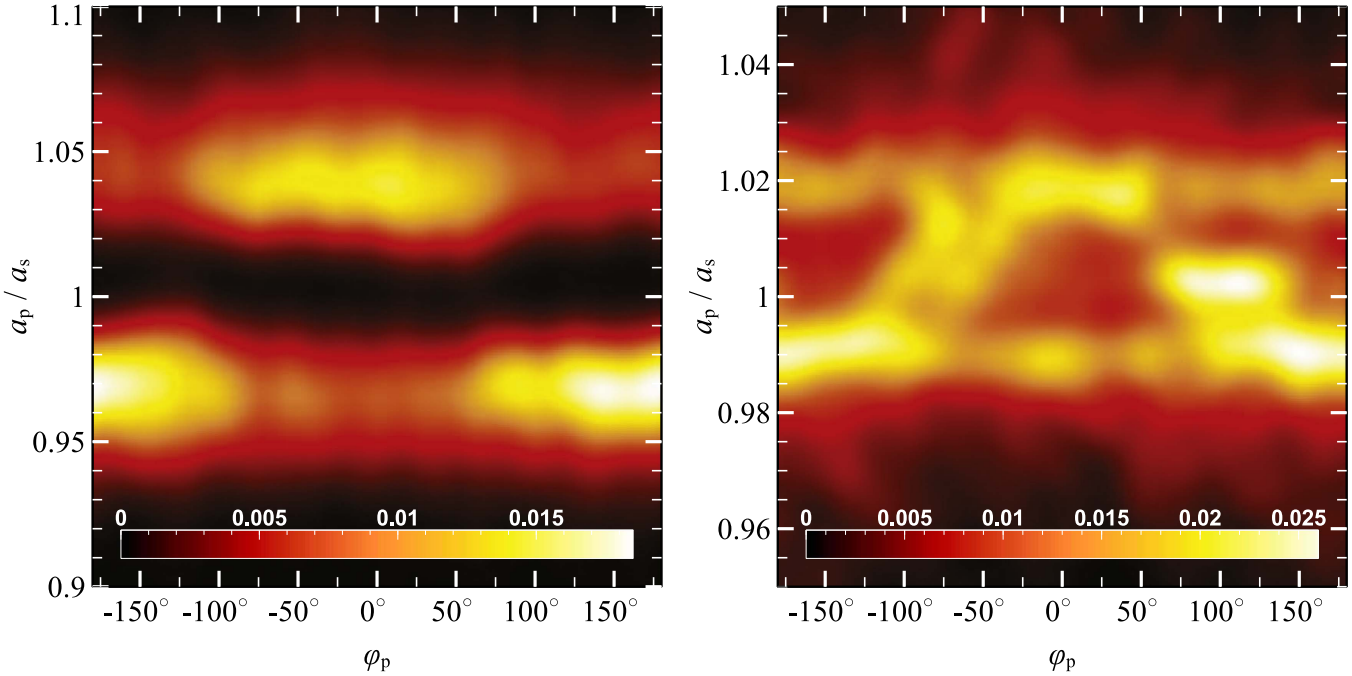

Figure 4. Probability density map of the ratio of the planetary semimajor axis a_p to that of the star a_s vs. the orbital phase φ_p of the planet around the star at the first stellar pericenter passage. $\varphi_p = 180°$ indicates that the planet is in between the SMBH and the star, while $\varphi_p = 0°$ indicates that the planet is in opposition with respect to the SMBH. Left panel: set A (coplanar prograde runs). Right panel: set B (coplanar retrograde runs).

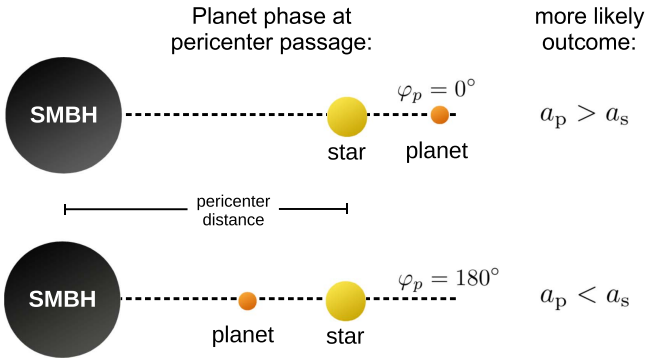

Figure 5. Schematic representation of two extreme orbital phases of the planet at the stellar pericenter passage, along with the more likely outcomes if the planet gets stripped from its parent star. a_p: semimajor axis of the planet with respect to the SMBH after it becomes unbound, a_s: semimajor axis of the parent star, φ: orbital phase of the planet at the stellar pericenter passage.

compare the orbital parameters of the captured planets with those of clouds G1 and G2.

4. DISCUSSION

4.1. Orbital Properties of Unbound Planets

As shown in Figure 3, planets remain on orbits similar to those of their parent star after being captured by the SMBH. This implies that the velocity kick induced by the SMBH is at least one order of magnitude less than the stellar orbital velocity. Furthermore, there is a gap in the distribution of the semimajor axes of captured planets in the prograde case.

Figure 4 (showing the ratio of semimajor axes a_p/a_s versus the orbital phase of the planet) suggests that planets escaping from L1 (inner Lagrangian point) end up on tighter orbits, while planets escaping from L2 (outer Lagrangian point) end up on looser orbits.

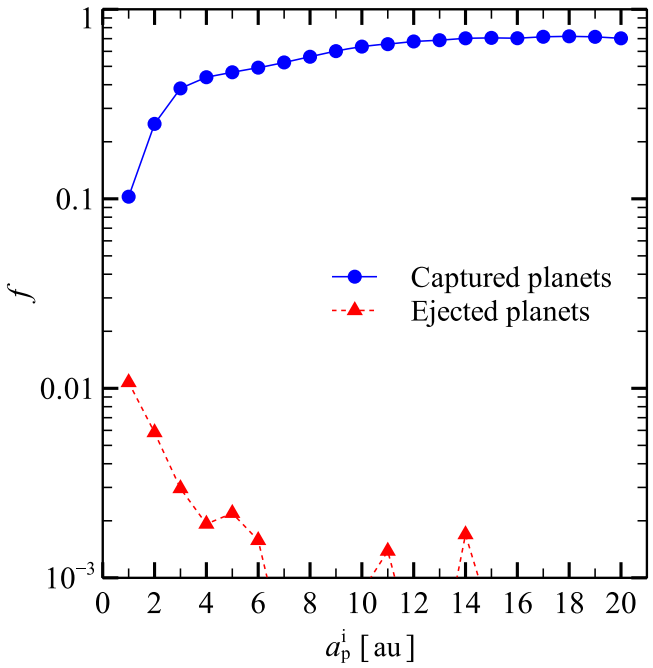

Figure 6. Fraction of captured and ejected planets as a function of the initial semimajor axis of the planetary orbit for all the S-star simulations. Blue solid line: fraction of unbound planets. Red dashed line: fraction of planets ejected from the system. Planets whose initial semimajor axis is larger than the Jacobi radius of the star at the initial conditions are not included in this figure.

Based on these considerations, we can estimate the changes in specific angular momentum and energy of the planet in the framework of the restricted three-body problem. We develop a simple analytic model based on three assumptions: (i) the planet becomes unbound during the stellar pericenter passage, (ii) the planet escapes the Hill sphere of the star from either the outer or the inner Lagrangian point, (iii) the velocity of the

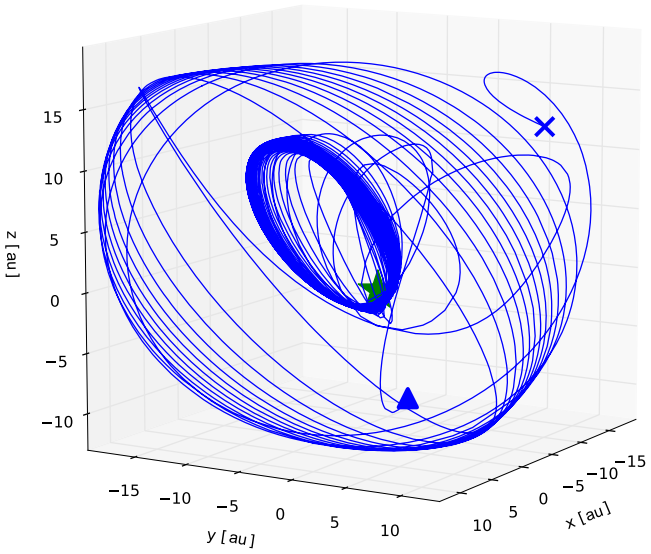

Figure 7. Trajectory of a planet around the star S19 of the S-star cluster, in the reference frame that corotates with the star. The initial semimajor axis of the planet is 10 au. Blue triangle: initial position of the planet. Blue cross: position of the planet at the time the planet becomes unbound with respect to the star (540 yr). Green star: position of the star. The SMBH is located along the negative x-axis, while the stellar tangential velocity is directed along the positive y-axis.

planet with respect to the rotating frame of reference at the moment of escape equals its orbital velocity $v_{\rm p}$. With these assumptions we can compute the difference in specific energy and angular momentum between the orbits of planet and star, ΔE and ΔL, respectively:

$$\Delta E = -\frac{G\,M_{\rm SMBH}}{p}\frac{r_{\rm J}}{p-r_{\rm J}} - v_{\rm s}^2\frac{r_{\rm J}}{p}\left(1-\frac{1}{2}\frac{r_{\rm J}}{p}\right)$$
$$\Delta L = -r_{\rm J}\,v_{\rm s} - p\,v_{\rm p} + r_{\rm J}\,v_{\rm p}, \quad (2)$$

where G is the gravitational constant, $M_{\rm SMBH}$ is the mass of the SMBH, p is the pericenter distance of the stellar orbit, $r_{\rm J}$ is the Jacobi radius at pericenter (Equation (1)), $v_{\rm s}$ is the stellar velocity at pericenter, and $v_{\rm p}$ is the orbital velocity of the planet. The sign of $r_{\rm J}$ and $v_{\rm p}$ is positive if the planet escapes from the inner Lagrangian point, negative if it escapes from the outer Lagrangian point, and $v_{\rm p}$ changes sign for retrograde orbits.

Figure 8 shows the variation of energy (ΔE) and angular momentum (ΔL) predicted from the analytic model compared to the simulations. In the case of prograde orbits (left panel, set A), the simple analytic model reproduces the bimodal energy distribution very well. The analytic model overestimates ΔE with decreasing pericenter distance, because the planet may escape before reaching the pericenter if the pericenter is very small. In contrast, the analytic model does not match the variation of energy and angular momentum in the simulations with retrograde orbits (right panel of Figure 8, set B).

Inserting the values drawn from the initial conditions of our simulations into Equations (1) and (2), we can evaluate the parameters of the new orbit of the planet around the SMBH. In Figure 3 we plot the predicted $a_{\rm p}/a_{\rm s}$ and $e_{\rm p}/e_{\rm s}$ along with the results of the simulations.

The predicted semimajor axis distribution matches the simulations in the case of prograde orbits (set A, Figure 3, left panel), reproducing the gap in this distribution. However, the analytic model also predicts a bimodality in the eccentricity distribution, which is not present in the simulations. In particular, the analytic model predicts that tighter orbits have mostly lower eccentricity and looser orbits have mostly higher eccentricity, while in the simulations we find mixed outcomes. This happens because the planet can escape before the star reaches its pericenter, thus invalidating assumption (i) of the analytic model. Moreover, 85% of the unbound planets begin the simulation outside $0.5r_{\rm J}$, so they may immediately become unbound and consequently violate all the assumptions of the analytic model.

The analytic model fails to predict the distribution of both semimajor axis and eccentricity in the case of retrograde orbits (set B, Figure 3, right panel). This occurs because the escape mechanism for retrograde orbits is different from that for prograde orbits. Just a small fraction of retrograde planets escape from one of the Lagrangian points (e.g., Figure 4). Moreover, planets in retrograde orbits can survive several stellar pericenter passages before being kicked into an unstable orbit, and the planetary escape may occur anywhere along the stellar orbit (see Figure 2, right panel).

Our results are consistent with the findings of Suetsugu & Ohtsuki (2013), who studied the orbital properties of planetesimals captured temporarily by a planet in a circular heliocentric orbit. Suetsugu & Ohtsuki (2013) highlight that captures of planetesimals into prograde orbits about the planet (i.e., through Lagrangian point L1 or L2) take place for a certain range of semimajor axes, leading to a gap in the semimajor axis distribution, whereas captures into retrograde orbits do not produce a significant gap.

4.2. Comparison with Orbits of Clouds G1 and G2

Figure 9 shows the probability density map of finding an unbound planet in the semimajor axis–eccentricity plane for the CW disk simulations. No planet can match the orbits of cloud G1 or G2. In particular, none of the simulated planets can achieve a highly eccentric orbit. In fact, the closest pericenter passage of an unbound planet in our simulations is 1750 au, a factor of ∼9 larger than the pericenter passage of cloud G1.

Since unbound planets remain on orbits similar to those of their parent star, we expect that they will experience scattering by the stars in the CW disk. Angular momentum diffusion and scattering in the CW disk may bring low-mass objects into nearly radial orbits (Murray-Clay & Loeb 2012). N-body simulations that include the entire CW disk are required to study this effect and will be presented in a forthcoming study (A. A. Trani et al. 2016, in preparation).

Figure 10 is the same as Figure 9 but for captured planets in the S-stars simulations. Most planets that have escaped from the S-stars are on highly eccentric orbits and are compatible with the clouds G1 and G2. In particular, we find that captured planets have probabilities of 2% and 70% of having semimajor axis and eccentricity within 1σ of the observations for G2 and G1.

We also study the inclination of the orbits of captured planets. Figure 11 shows the probability density map of finding an unbound planet in the pericenter distance–inclination plane for the S-star simulations. Since captured planets retain approximately the same inclination as their parent star, each blob corresponds to one or more S-stars.

None of the simulated planets has exactly the same inclination of its orbit as G2 and G1. Although planets that

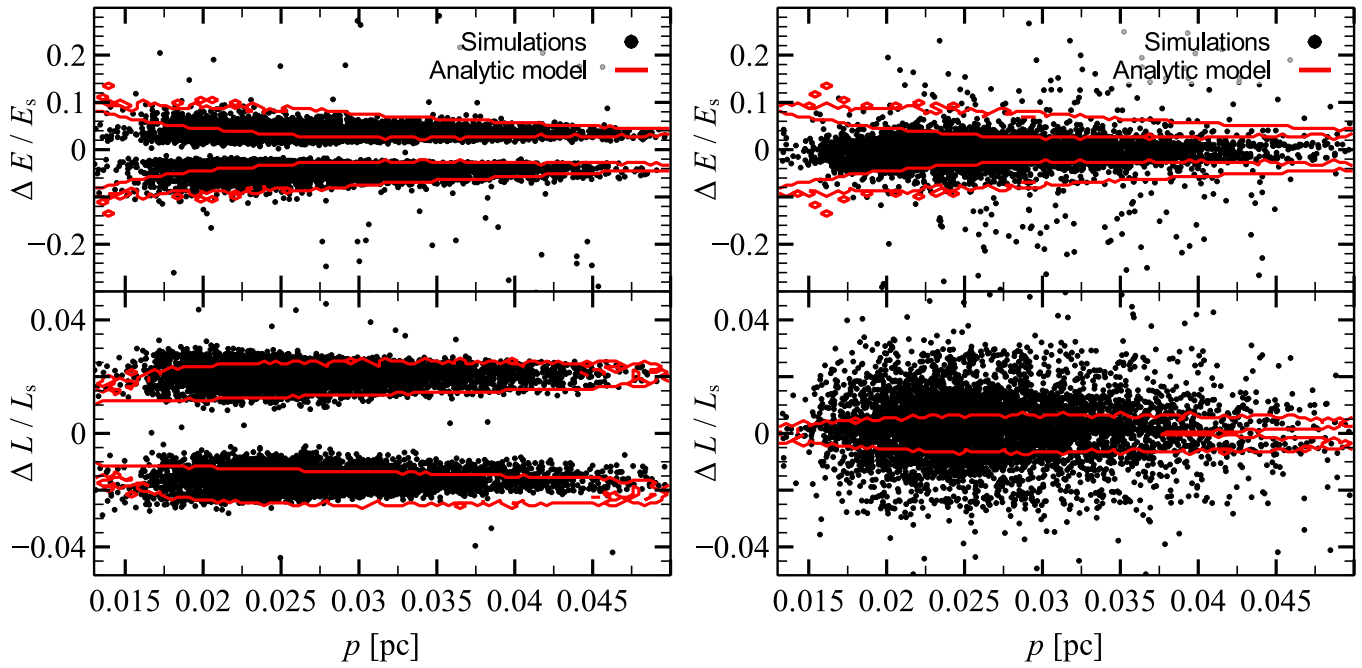

Figure 8. Top (bottom) panels: difference in energy (angular momentum) between the orbits of planet and star around the SMBH as a function of the pericenter distance of the stellar orbit, normalized to the energy (angular momentum) of the star. Black dots:results of the simulations. Red contours: predictions of the analytic model (Equations (2)). Left panel: set A (coplanar prograde runs). Right panel: set B (coplanar retrograde runs).

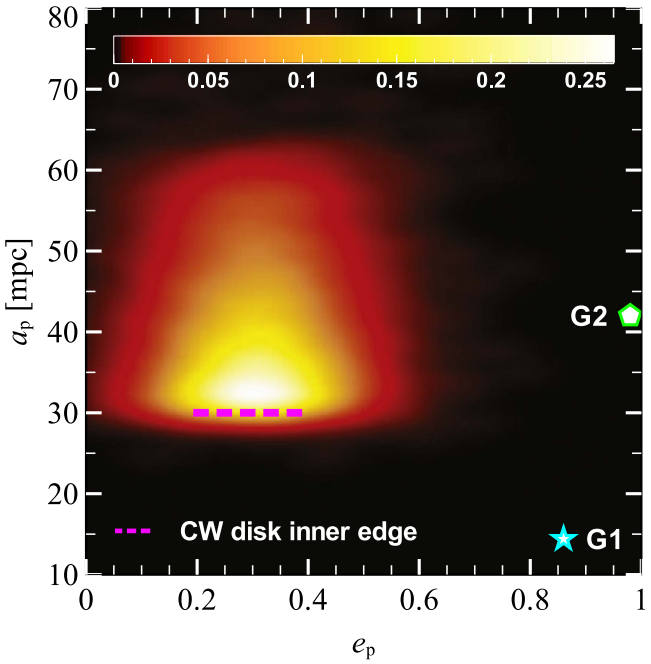

Figure 9. Probability density map of semimajor axis and eccentricity of captured planets in the CW disk simulations. Green pentagon: cloud G2. Cyan star: cloud G1. Magenta dashed line: inner edge of the CW disk. All simulated sets were used.

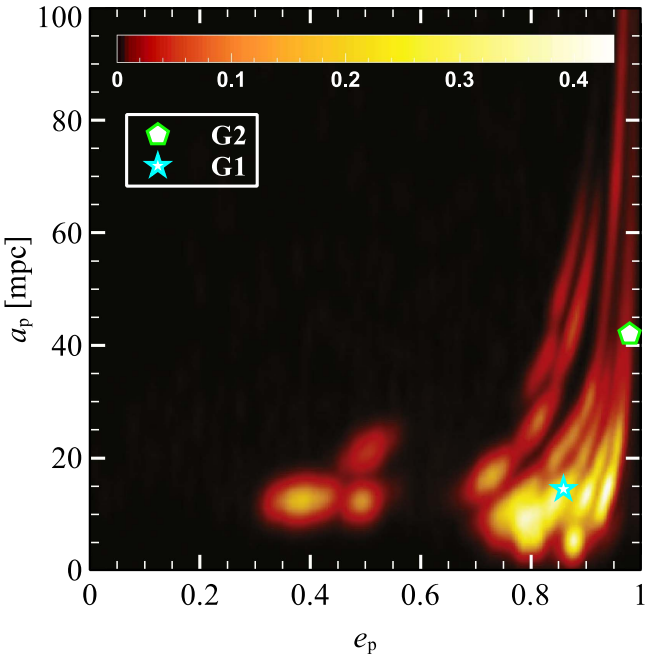

Figure 10. Probability density map of semimajor axis and eccentricity of the captured planets in the S-stars simulations. Green pentagon: cloud G2. Cyan star: cloud G1.

have escaped from S29 lie very close to the position of G2 in the $p-i$ plane, further analysis reveals that the longitude of the ascending node Ω mismatches by $\sim 75°$; therefore the orbit of G2 and that of the planets that have escaped from S29 do not lie in the same plane. However, the orbital properties of several S-stars are still unconstrained (Gillessen et al. 2009). Many S-stars fainter than $m_H > 19$ are not even detected. Identifying more S-stars and deriving their orbital properties (especially their inclinations) will provide important clues for our scenario.

Moreover, explaining G1 and G2 with this scenario requires that planets can exist around S-stars. One of the most popular scenarios to explain the formation of the S-stars, the so-called binary breakup scenario (Perets et al. 2009) predicts that the S-stars were captured by the SMBH via the Hills mechanism

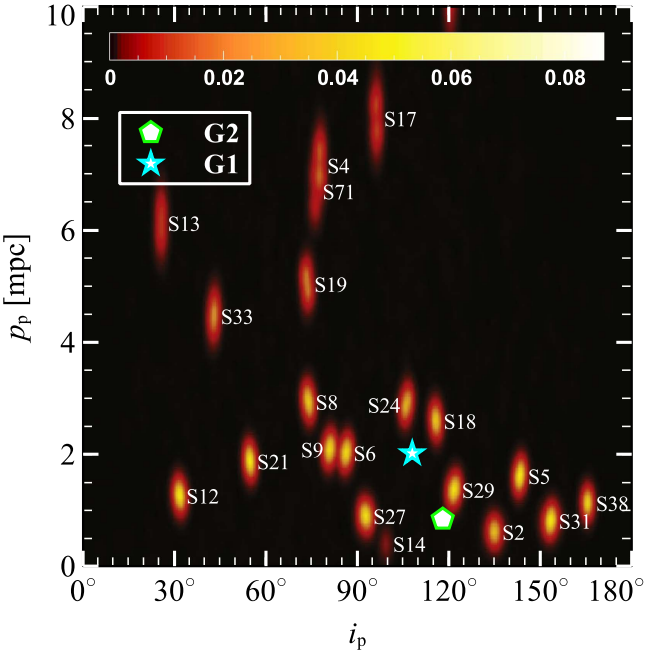

Figure 11. Probability density map of pericenter distance and inclination of captured planets in the S-stars simulations. Green pentagon: cloud G2. Cyan star: cloud G1. Each blob corresponds to the planets that have escaped from a single S-star, labeled on the map.

during encounters with binary stars. A protoplanetary disk might be disrupted during the binary encounter with the SMBH. Alternatively, the planet might have been formed around the S-star before it was captured by the SMBH. Ginsburg et al. (2012) showed that some planets will likely remain bound to their star during a three-body encounter, if their semimajor axis is $a_p^i \gtrsim 0.5$ au, since planets with $a_p^i \lesssim 0.5$ au are more likely to be ejected from the system. However, the closer the planet to the S-star, the more difficult it is for the SMBH to capture it. All these issues deserve further study.

Finally, we note that our simulations were done for a star–planet system, but our results can be generalized also to a star–star system. In other words, a low-mass star initially bound to an S-star might have been captured by the SMBH into a new orbit, matching the eccentricity and semimajor axis of G1 and G2.

5. CONCLUSIONS

We investigated the dynamics of planets orbiting the young stars in the inner edge of the CW disk and in the S-star cluster by means of regularized N-body simulations. We simulated 4×10^4 hierarchical systems consisting of a SMBH, a star, and its planet lying in the CW disk. We also ran 2×10^4 N-body realizations of the 27 innermost S-stars, assigning a planet to each S-star.

The planet may escape its parent star and be tidally captured by the SMBH, depending on the properties of the orbit of the star and the planet. Planets on retrograde (prograde) orbits are captured if their orbit lies outside r_J ($0.5r_J$), where r_J is the Jacobi radius.

We study the orbital properties of starless planets around the SMBH and find that planets remain on orbits similar to those of their parent star. In particular, we find that in 95% of the runs the semimajor axis and eccentricity of the planetary orbit differ by less than 6% and 13% from those of the parent star, respectively.

In case of prograde coplanar orbits, the semimajor axis of starless planets can be approximately predicted using a simple analytic model. We show that the escape mechanism of the planet from the Hill sphere of the parent star determines the semimajor axis of the planet: if the planet escapes from the inner Lagrangian point (i.e., the one located toward the SMBH) it will end up on a tighter orbit; in contrast, if it escapes from the outer Lagrange point it will end up on a looser orbit. Furthermore, we find that looser orbits tend to have higher eccentricity than the orbit of the parent star, while tighter orbits tend to have lower eccentricity.

In the case of planets in the CW disk, we find that the closest passage to the SMBH achieved by a starless planet is at 1750 au, a factor ∼9 larger than the pericenter distance of the orbit of cloud G2. We speculate that perturbations from other stars in the CW disk may bring planets into nearly radial orbits. In forthcoming studies we will investigate the effect of angular momentum transport and scatterings on the dynamics of planets in the CW disk.

In contrast, the semimajor axis and eccentricity of planets escaping from the S-stars can match those of G1 and G2. The main issue is that the orbital planes of known S-stars do not match those of G1 and G2. Therefore, future detections of S-stars with approximately the same orbital plane as G1 and G2 are essential to support this scenario. We note that our simulations were run for star–planet systems, but our predictions apply to any low-mass companions of the CW disk stars or of the S-stars. Thus, our scenario also predicts that G1 and G2 might be low-mass stars that were previously bound to S-stars.

We thank the referee, Keiji Ohtsuki, for his careful reading of the manuscript and for his invaluable comments that improved the manuscript. The authors acknowledge financial support from INAF through grant PRIN-2014-14. M.M. and M.S. acknowledge financial support from the Italian Ministry of Education, University and Research (MIUR) through grant FIRB 2012 RBFR12PM1F. M.M. acknowledges financial support from the MERAC Foundation. We thank Alessandro Ballone for useful and stimulating discussions.

APPENDIX
CLASSIFICATION OF PLANETARY ORBITS

Temporary planetary orbits around the star (before tidal capture by the SMBH) can be classified according to Suetsugu et al. (2011), who studied the orbital properties of planetesimals captured temporarily by a planet in a circular heliocentric orbit. They distinguish four types of orbits—three for retrograde orbits and one for prograde—and find that the type of orbit depends on the eccentricity and energy of the planetesimal orbit around the Sun.

We find that most prograde orbits of set A are of type H (Hill sphere-shaped, left panel of Figure 12), which is typical of low-energy orbits that remain confined inside the Hill sphere, with escapes mainly occurring through the Lagrangian points. On the other hand, most retrograde orbits of set B are of type A (apple-shaped, right panel of Figure 12). Planets on type A orbits can orbit past the Hill sphere of the star without escaping.

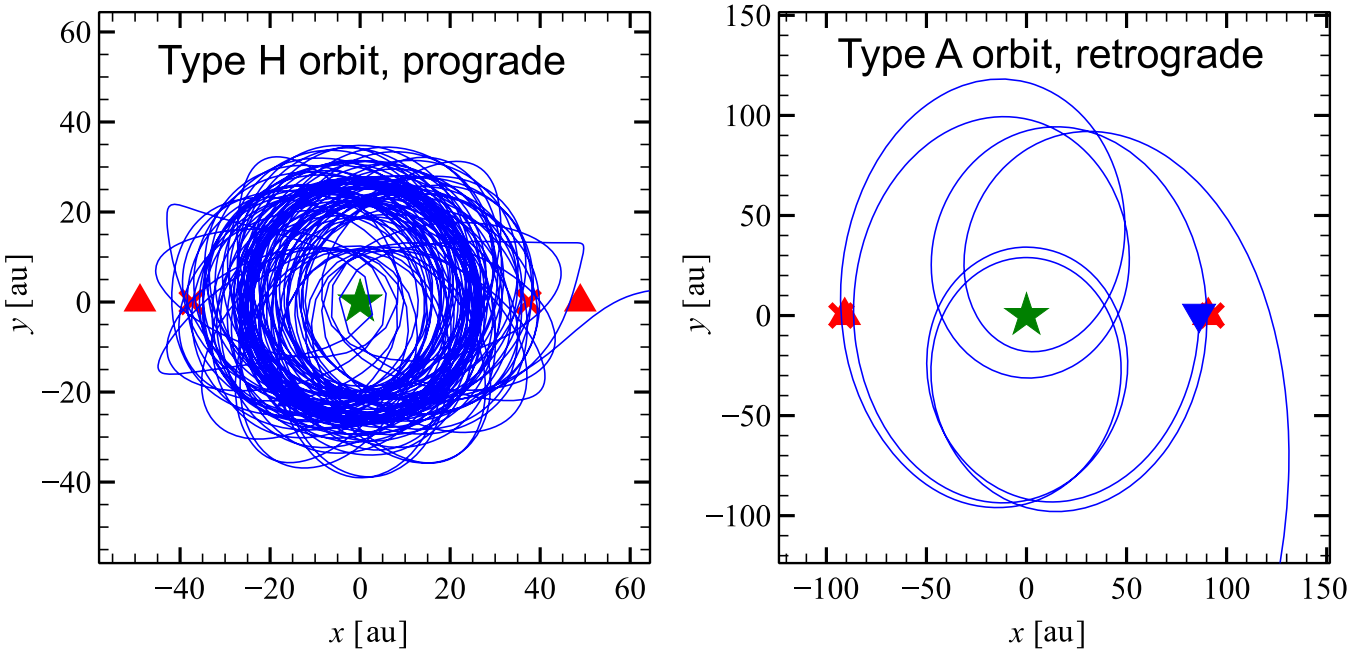

Figure 12. Same as Figure 2, but for two different realizations. Left panel: simulation from set A (coplanar prograde) that we classify as type H (Suetsugu et al. 2011). Right panel: simulation from set B (coplanar retrograde) that we classify as type A (Suetsugu et al. 2011).

Escapes occur mainly in the SMBH–star direction but not strictly through the Lagrangian points.

We do not find any evidence of type R and E orbits in our simulations. These orbit types were found by Suetsugu et al. (2011) in the case of high velocity dispersion between the planet and the planetesimal. The dispersion-dominated velocity regime is excluded by construction in our case, since the planet is initially bound to the star.

We note that many orbits we examined are irregular and do not resemble any of the aforementioned orbit types. This is due to the eccentricity of the stellar orbit, which makes the tidal field experienced by the planet not stationary, unlike in the zero-eccentricity study of Suetsugu et al. (2011). This leads to an additional perturbation that can modify the shape of the planetary orbit, and may cause earlier escape than in the zero-eccentricity case.

REFERENCES

Aarseth, S. J. 2003, Gravitational N-Body Simulations (Cambridge: Cambridge University Press)
Alig, C., Burkert, A., Johansson, P. H., & Schartmann, M. 2011, MNRAS, 412, 469
Alig, C., Schartmann, M., Burkert, A., & Dolag, K. 2013, ApJ, 771, 119
Ballone, A., Schartmann, M., Burkert, A., et al. 2013, ApJ, 776, 13
Bartko, H., Martins, F., Fritz, T. K., et al. 2009, ApJ, 697, 1741
Bonnell, I. A., & Rice, W. K. M. 2008, Sci, 321, 1060
Burkert, A., Schartmann, M., Alig, C., et al. 2012, ApJ, 750, 58
Čadež, A., Calvani, M., & Kostić, U. 2008, A&A, 487, 527
Calderón, D., Ballone, A., Cuadra, J., et al. 2016, MNRAS, 455, 4388
Capuzzo-Dolcetta, R., Spera, M., & Punzo, D. 2013, JCoPh, 236, 580
Clénet, Y., Rouan, D., Gratadour, D., et al. 2005, A&A, 439, L9
De Colle, F., Raga, A. C., Contreras-Torres, F. F., & Toledo-Roy, J. C. 2014, ApJL, 789, L33
Do, T., Lu, J. R., Ghez, A. M., et al. 2013, ApJ, 764, 154
Eckart, A., Mužić, K., Yazici, S., et al. 2013, MmSAI, 84, 618
Ghez, A. M., Duchêne, G., Matthews, K., et al. 2003, ApJL, 586, L127
Ghez, A. M., Hornstein, S. D., Lu, J. R., et al. 2005, ApJ, 635, 1087
Gillessen, S., Eisenhauer, F., Trippe, S., et al. 2009, ApJ, 692, 1075
Gillessen, S., Genzel, R., Fritz, T. K., et al. 2011, Natur, 481, 51
Gillessen, S., Genzel, R., Fritz, T. K., et al. 2013a, ApJ, 763, 78
Gillessen, S., Genzel, R., Fritz, T. K., et al. 2013b, ApJ, 774, 44
Ginsburg, I., Loeb, A., & Wegner, G. A. 2012, MNRAS, 423, 948
Guillochon, J., Loeb, A., MacLeod, M., & Ramirez-Ruiz, E. 2014, ApJL, 786, L12
Hamers, A. S., & Portegies Zwart, S. F. 2015, MNRAS, 446, 710
Hamilton, D. P., & Burns, J. A. 1991, Icar, 92, 118
Hamilton, D. P., & Burns, J. A. 1992, Icar, 96, 43
Hobbs, A., & Nayakshin, S. 2009, MNRAS, 394, 191
Kostić, U., Čadež, A., Calvani, M., & Gomboc, A. 2009, A&A, 496, 307
Lu, J. R., Do, T., Ghez, A. M., et al. 2013, ApJ, 764, 155
Lu, J. R., Ghez, A. M., Hornstein, S. D., et al. 2009, ApJ, 690, 1463
Lucas, W. E., Bonnell, I. A., Davies, M. B., & Rice, W. K. M. 2013, MNRAS, 433, 353
Mapelli, M., & Gualandris, A. 2016, in Lecture Notes in Physics, Vol. 905 ed. F. Haardt et al. (Berlin: Springer), 205
Mapelli, M., Hayfield, T., Mayer, L., & Wadsley, J. 2008, arXiv:0805.0185
Mapelli, M., Hayfield, T., Mayer, L., & Wadsley, J. 2012, ApJ, 749, 168
Mapelli, M., & Ripamonti, E. 2015, ApJ, 806, 197
Mapelli, M., & Trani, A. A. 2016, A&A, 585, A161
Meyer, F., & Meyer-Hofmeister, E. 2012, A&A, 546, L2
Mikkola, S., & Tanikawa, K. 1999a, MNRAS, 310, 745
Mikkola, S., & Tanikawa, K. 1999b, CeMDA, 74, 287
Miralda-Escudé, J. 2012, ApJ, 756, 86
Murray-Clay, R. A., & Loeb, A. 2012, NatCo, 3, 1049
Paumard, T., Genzel, R., Martins, F., et al. 2006, ApJ, 643, 1011
Perets, H. B., Gualandris, A., Kupi, G., Merritt, D., & Alexander, T. 2009, ApJ, 702, 884
Pfuhl, O., Gillessen, S., Eisenhauer, F., et al. 2015, ApJ, 798, 111
Phifer, K., Do, T., Meyer, L., et al. 2013, ApJL, 773, L13
Prodan, S., Antonini, F., & Perets, H. B. 2015, ApJ, 799, 118
Schartmann, M., Burkert, A., Alig, C., et al. 2012, ApJ, 755, 155
Schodel, R., Ott, T., Genzel, R., et al. 2003, ApJ, 596, 1015
Scoville, N., & Burkert, A. 2013, ApJ, 768, 108
Shcherbakov, R. V. 2014, ApJ, 783, 31
Stoer, J., & Bulirsch, R. 2002, Introduction to Numerical Analysis (New York: Springer), doi:10.1007/978-0-387-21738-3
Suetsugu, R., & Ohtsuki, K. 2013, MNRAS, 431, 1709
Suetsugu, R., Ohtsuki, K., & Tanigawa, T. 2011, AJ, 142, 200
Trani, A. A., Mapelli, M., Bressan, A., et al. 2016, ApJ, 818, 29
Williams, J. P., & Cieza, L. A. 2011, ARA&A, 49, 67
Witzel, G., Ghez, A. M., Morris, M. R., et al. 2014, ApJL, 796, L8
Yelda, S., Ghez, A. M., Lu, J. R., et al. 2014, ApJ, 783, 131
Yusef-Zadeh, F., Roberts, D. A., Wardle, M., et al. 2015, ApJL, 801, L26
Zubovas, K., Nayakshin, S., & Markoff, S. 2012, MNRAS, 421, 1315